Geographic correlation between hot spots and deep mantle lateral shear-wave velocity gradients

Michael S. Thorne [a,*], Edward J. Garnero [a], Stephen P. Grand [b]

[a] *Department of Geological Sciences, Arizona State University, Tempe, AZ 85287, USA*
[b] *Department of Geological Sciences, University of Texas at Austin, Austin, TX 78712, USA*

Abstract

Hot spot volcanism may originate from the deep mantle in regions exhibiting the Earth's most pronounced lateral S-wave velocity gradients. These strong gradient regions display an improved geographic correlation over S-wave velocities to surface hot spot locations. For the lowest velocities or strongest gradients occupying 10% of the surface area of the core–mantle boundary (CMB), hot spots are nearly twice as likely to overlie the anomalous gradients. If plumes arise in an isochemical lower mantle, plume initiation should occur in the hottest (thus lowest velocity) regions, or in the regions of strongest temperature gradients. However, if plume initiation occurs in the lowest velocity regions of the CMB lateral deflection of plumes or plume roots are required. The average lateral deflections of hot spot root locations from the vertical of the presumed current hot spot location ranges from ∼300 to 900 km at the CMB for the 10–30% of the CMB covered by the most anomalous low S-wave velocities. The deep mantle may, however, contain strong temperature gradients or be compositionally heterogeneous, with plume initiation in regions of strong lateral S-wave velocity gradients as well as low S-wave velocity regions. If mantle plumes arise from strong gradient regions, only half of the lateral deflection from plume root to hot spot surface location is required for the 10–30% of the CMB covered by the most anomalous strong lateral S-wave velocities. We find that strong gradient regions typically surround the large lower velocity regions in the base of the mantle, which may indicate a possible chemical, in addition to thermal, component to these regions.
© 2004 Elsevier B.V. All rights reserved.

Keywords: Hot spot; Mantle plume; Seismic tomography; Mantle convection

1. Introduction

1.1. Seismic evidence for mantle plumes

Morgan (1971) first proposed that hot spots may be the result of thermal plumes rising from the core–mantle boundary (CMB). This plume hypothesis has gained widespread appeal, yet direct seismic imaging of whole mantle plumes through travel-time tomography or forward body wave studies have not yet resolved this issue (e.g., Ji and Nataf, 1998b; Nataf, 2000). Plume conduits are predicted to be on the order of 100–400 km in diameter, with maximum temperature anomalies of roughly 200–400 K (Loper and Stacey, 1983; Nataf and Vandecar, 1993; Ji and Nataf, 1998a). Global tomographic models typically possess lower resolution than is necessary to detect a plume in its entirety. Table 1 lists the resolution for several recent whole mantle tomographic models. However, a few higher resolution tomographic studies have inferred uninterrupted low velocities from

* Corresponding author.
E-mail address: mthorne@asu.edu (M.S. Thorne).

Table 1
S-wave velocity models analyzed in this study

Model	Lateral parameterization	Lateral dimensions	Radial parameterization	Reference
SAW12D	Spherical harmonics	Up to 12° (∼1800 km[a])	Legendre polynomials	Li and Romanowicz (1996)
S14L18	Equal area blocks	4° × 4° (∼240 km[a])	200 km thick deepest layer	Masters et al. (2000)
Kuo12	Spherical harmonics	Up to 12° (∼1800 km[a])	One layer 250 km thick	Kuo et al. (2000)
S20RTS	Spherical harmonics	Up to 20° (∼1000 km[a])	21 Vertical splines	Ritsema and van Heijst (2000)
S362C1	Spherical B splines	Roughly 18° (∼1200 km[a])	14 cubic B splines	Gu et al. (2001)
TXBW	Equal area blocks	∼2.5° × ∼2.5° (∼150 km[a])	240 km thick deepest layer	Grand (2002)

[a] Approximate resolution at CMB.

the CMB to the base of the crust. For example, the models of Bijwaard and Spakman (1999) (65–200 and 150–400 km lateral resolution in upper and lower mantle, respectively) and Zhao (2001) (5° lateral resolution) both show uninterrupted low P-wave velocities beneath Iceland, which have been interpreted as evidence for a whole mantle plume in the region. In addition, the tomographic model S20RTS (Ritsema et al., 1999; Ritsema and van Heijst, 2000) shows a low S-wave velocity anomaly in the upper mantle beneath Iceland that ends near 660 km depth. High resolution (e.g., block sizes of 75 km × 75 km × 50 km (Foulger et al., 2001)) regional tomographic studies have also been used to image plumes in the upper mantle and have shown that some plumes extend at least as deep as the transition zone, but the full depth extent of the inferred plumes remains unresolved (Wolfe et al., 1997; Foulger et al., 2001; Gorbatov et al., 2001). Resolution at even shorter scale lengths is necessary to determine with greater confidence any relationship between continuity of low velocities in the present models and mantle plumes.

Several body wave studies have focused on plume-like structures related to hot spots at the base of the mantle. For example, Ji and Nataf (1998b) used a method similar to diffraction tomography to image a low velocity anomaly northwest of Hawaii that rises at the base of the mantle and extends at least 1000 km above the CMB. Helmberger et al. (1998) used waveform modeling to show evidence for a 250 km wide dome-shaped, ultra-low velocity zone (ULVZ) structure beneath the Iceland hot spot at the CMB. Ni et al. (1999) used waveform modeling to confirm the existence of an anomalous (approximately up to −4% δV_s) low velocity structure beneath Africa extending upward 1500 km from the CMB, which may be

related to one or more of the hot spots found in the African region. Several seismic studies have shown evidence for plumes in the mantle transition zone (410–660 km), suggesting that hot spots may feed plumes at a minimum depth of the uppermost lower mantle (Nataf and Vandecar, 1993; Wolfe et al., 1997; Foulger et al., 2001; Niu et al., 2002; Shen et al., 2002). These plumes are not necessary to explain the majority of hot spots on Earth's surface (Clouard and Bonneville, 2001), but suggest that some hot spots may be generated from shallow upwelling as implied by layered convection models (e.g., Anderson, 1998).

1.2. Indirect evidence: correlation studies

The inference that the deepest mantle seismic structure is related to large-scale surface tectonics has been given much attention in the past decade (e.g., Bunge and Richards, 1996; Tackley, 2000). Several studies suggest that past and present surface subduction zone locations overlay deep mantle high seismic wave speeds (Dziewonski, 1984; Su et al., 1994; Wen and Anderson, 1995), which are commonly attributed to cold subducting lithosphere migrating to the CMB. Recent efforts in seismic tomography have revealed images of planar seismically fast structures resembling subducting lithosphere that may plunge deep into the mantle (Grand, 1994; Grand et al., 1997; van der Hilst et al., 1997; Bijwaard et al., 1998; Megnin and Romanowicz, 2000; Gu et al., 2001). The final depth of subduction has far reaching implications for the nature of mantle dynamics and composition (Albarede and van der Hilst, 2002). This finding, coupled with the spatial correlation of hot spots and deep mantle low seismic velocities, are main constituents of the argument for whole mantle convection (Morgan,

1971; Hager et al., 1985; Ribe and Devalpine, 1994; Su et al., 1994; Grand et al., 1997; Lithgow-Bertelloni and Richards, 1998).

With present challenges in direct imaging of mantle plumes or the source of hot spots, comparison studies of hot spots and deep mantle phenomena have yielded provocative results. Surface locations of hot spots have been correlated to low velocities (e.g., Wen and Anderson, 1997; Seidler et al., 1999) and UL-VZs (Williams et al., 1998) at the CMB. It has also been noted, however, that the locations of hot spots at Earth's surface tend to lie near edges of low-velocity regions, as shown by tomographic models at the CMB (Castle et al., 2000; Kuo et al., 2000). This correlation has been used to imply that mantle plumes can be deflected by more than 1000 km from their proposed root source of the deepest mantle lowest velocities to the surface, perhaps by the action of "mantle winds" (e.g., Steinberger, 2000).

1.3. Other mantle plume studies

The wide variability of observed and calculated hot spot characteristics implies that several mechanisms for hot spot genesis may be at work. Modeling of plume buoyancy flux has been carried out for several hot spots (Davies, 1988; Sleep, 1990; Ribe and Christensen, 1994), revealing a wide range in the volcanic output of plumes possibly responsible for many hot spots. Geodynamic arguments suggest some hot spots may be fed by shallow-rooted (e.g., Albers and Christensen, 1996) or mid-mantle-rooted (e.g., Cserepes and Yuen, 2000) plume structures. Geochemical evidence suggests that different hot spot source regions may exist (Hofmann, 1997), as shown by isotopic studies that argue for either transition zone (e.g., Hanan and Graham, 1996) or CMB (e.g., Brandon et al., 1998; Hart et al., 1992) source regions. Further tomographic evidence has been used to argue that several hot spots may be fed by a single large upwelling from the deep mantle (e.g., Goes et al., 1999). Hence, the original mantle plume hypothesis (Morgan, 1971), that long-lived thermal plumes rise from the CMB, has expanded to include a wide variety of possible origins of hot spot volcanism.

In this study, we explore statistical relationships between the surface locations of hot spots and seismic heterogeneity observed in the deep mantle. Specifically, we compare hot spot surface locations to low S-wave velocity heterogeneities and strong S-wave lateral velocity gradients. We evaluate the origin of hot spot related plumes, and examine the implications for deep mantle composition and dynamics.

2. Calculation of lateral shear-wave velocity gradients

We analyzed gradients in lateral S-wave velocity at the CMB for six global models of S-wave velocities. Table 1 summarizes the parameterizations of each of the models analyzed. Using bi-cubic interpolation, we resampled models originally parameterized in either spherical harmonics or blocks onto a $1° \times 1°$ grid. Additionally, we smoothed block models laterally by Gaussian cap averaging with a radius of $4°$ or $8°$ for comparison with the smoother structures represented by spherical harmonics. We calculated lateral S-wave velocity gradients for the deepest layer in each model at every grid point as follows: (a) great circle arc segments were defined with 500–2000 km lengths centered on each grid point for every $5°$ of rotation in azimuth; (b) seismic velocity was estimated at 2, 3, 5, 7, or 9 equally spaced points (by nearest grid point interpolation) along each arc; (c) a least squares best fit line through arc sampling points was applied for each azimuth; and (d) the maximum slope, or gradient, and associated azimuth was calculated for each grid point. This approach proved versatile for computing lateral velocity gradients for the variety of model parameterizations analyzed (Table 1).

In order to compare S-wave velocities and lateral S-wave velocity gradients between different models, lower mantle S-wave velocities and lateral S-wave velocity gradients were re-scaled according to CMB surface area. For example, for model S20RTS, S-wave velocities at or lower than $\delta V_s = -1.16$, 10% of the surface area of the CMB is covered (herein after referred to as "% CMB surface area coverage"). Similarly, the most anomalous velocities occupying 20% CMB surface area coverage, are lower than $\delta V_s = -0.59$. Lateral S-wave velocity gradients are scaled in the same manner, where 10% CMB surface area coverage corresponds to the most anomalous strong gradients. The number of hot spots located within a given percentage of CMB surface area coverage for low

Table 2
Hot spots used with locations (after Steinberger, 2000)

Hot spot	Latitude	Longitude	Hot spot	Latitude	Longitude
1. Azores	38.5	−28.4	23. Kerguelen	−49.0	69.0
2. Balleny	−66.8	163.3	24. Lord Howe	−33.0	159.0
3. Bowie	53.0	−135.0	25. Louisville	−51.0	−138.0
4. Cameroon	4.2	9.2	26. Macdonald	−29.0	−140.2
5. Canary	28.0	−18.0	27. Marion	−46.9	37.8
6. Cape Verde	15.0	−24.0	28. Marquesas	−11.0	−138.0
7. Caroline	5.0	164.0	29. Meteor	−52.0	1.0
8. Cobb	46.0	−130.0	30. New England	28.0	−32.0
9. Comores	−11.8	43.3	31. Pitcairn	−25.0	−129.0
10. Darfur	13.0	24.0	32. Raton	37.0	−104.0
11. East Africa	6.0	34.0	33. Reunion	−21.2	55.7
12. East Australia	−38.0	143.0	34. St. Helena	−17.0	−10.0
13. Easter	−27.1	−109.3	35. Samoa	−15.0	−168.0
14. Eifel	50.0	7.0	36. San Felix	−26.0	−80.0
15. Fernando	−4.0	−32.0	37. Socorro	18.7	−111.0
16. Galapagos	−0.4	−91.5	38. Tahiti	−17.9	−148.1
17. Guadelupe	27.0	−113.0	39. Tasmanid	−39.0	156.0
18. Hawaii	19.4	−155.3	40. Tibesti	21.0	17.0
19. Hoggar	23.0	6.0	41. Trindade	−20.5	−28.8
20. Iceland	65.0	−19.0	42. Tristan	−38.0	−11.0
21. Jan Mayen	71.1	−8.2	43. Vema	−33.0	4.0
22. Juan Fernandez	−34.0	−82.0	44. Yellowstone	44.6	110.5

S-wave velocity or strong lateral gradient are tabulated into hot spot hit counts. In this manner, the spatial distribution of the most anomalous low seismic velocities and strong gradients can be equally compared and correlated to hot spots. For example, the first two columns of Fig. 2 show velocities and gradients of the model S20RTS (Ritsema and van Heijst, 2000), with contours drawn in green around the 10, 20, and 30% most anomalously low shear velocities and strongest lateral S-wave velocity gradients scaled by CMB surface area coverage. In the third column (Fig. 2), the % CMB surface area coverage contours are filled in solid, with hot spot positions drawn as red circles and hot spot hit counts listed beneath the respective globes.

In order to compare shear velocities and our computed lateral S-wave velocity gradients to hot spot surface locations, we used a catalog of 44 hot spots (Steinberger, 2000). We used this catalog because it imposed three stringent conditions to qualify as a hot spot. First, each hot spot location must be associated with a volcanic chain, or at least two age determinations must exist indicating a volcanic history of several million years. Second, two out of four of the follow-

ing conditions must be met: (i) present-day or recent volcanism (ii) distinct topographic elevation (iii) associated volcanic chain, or (iv) associated flood basalt. Third, all subduction zone related volcanism was excluded as being related to hot spots. Table 2 and Fig. 1 show the hot spots and their respective locations used in this study.

This is not a comprehensive list of all possible hot spots (e.g., compare with 19 hot spots of Morgan (1972), 37 of Sleep (1990) or 117 of Vogt (1981)). Also, we do not presume that plumes rooted in the CMB necessarily produce each of these hot spots. As noted by Steinberger (2000), this list does not include any hot spots in Asia due to difficulty in recognition. Therefore, Table 2 gives a representative group of Earth's most prominent hot spots.

3. Results

For the 10% of the CMB surface area covered by lowest velocities or strongest gradients, nearly twice as many hot spots are found within 5° of strong gradients. For example, this observation is apparent in the third
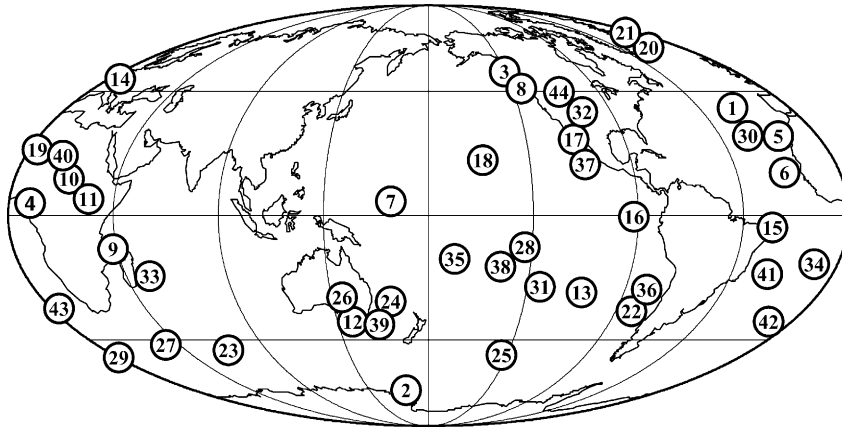
Fig. 1. Locations of hot spots used in this study are plotted as closed circles. Numbers correspond to the number listed next to each hot spot in Tables 2–4.

column of Fig. 2 for model S20RTS. In this model, 23 hot spots—over half of all hot spots—overlie the strongest gradients, compared to 12 hot spots for low velocities. At 20% CMB surface area coverage 22 hot spots (50%) are found over low velocities, whereas 35 (~80%) are found over strong gradients. Increasing the coverage to greater than one-fourth of the CMB decreases this disparity. For example, for 30% of the CMB covered by lowest velocities or strongest gradients, model S20RTS has ~61% of all hot spots over the lowest velocities and ~84% over the strongest gradients. The most striking disparity in hot spot hit count is seen in the 10–40% CMB surface area coverage range, which holds for all models analyzed.

Fig. 3 displays the six models analyzed in this study. The first column of Fig. 3 displays the S-wave velocity perturbations, while the second and third columns show low S-wave velocity and strong lateral gradient, respectively, contoured and shaded on the basis of CMB surface area coverage. The number of hot spots located within a surface area contour for low shear velocity or strong lateral gradient are tabulated into hot spot hit counts, incrementing CMB surface area coverage in 1% intervals. In computing hot spot correlations to these distributions, we allowed for hot spot root lateral deflections by experimenting with a variable radius search bin centered on each hot spot to tabulate lowest velocity or strongest gradient within. Fig. 4 displays the hot spot hit counts for the model S20RTS, for a 5° radius search bin (approximately

300 km radius centered on each hot spot). Steinberger (2000) determined hot spot root locations due to mantle winds using three tomographic models, and estimated average lateral deflections from present day hot spot surface locations averaging ~12° (~734 km) at the CMB. A 5° radius search bin is the largest used in our calculations, which corresponds to less than half of this. However, Steinberger (2000) assumed a thermal origin to seismic heterogeneity, with the result of hot spot roots being located near the hottest temperatures and thus near the lowest velocities. We will first address the statistical correlations between hot spots and low S-wave velocities and then hot spots and strong gradients, and further discuss possible scenarios that relate to the origin of lower mantle heterogeneity.

4. Discussion

The number of hot spots nearest the strongest velocity gradients is significantly greater than for the lowest velocities in the deep mantle. This is demonstrated in Fig. 2 for model S20RTS, and is also seen in Fig. 4 which shows hot spot hit counts for either velocities or gradients versus percent coverage of the CMB for this model. Fig. 4 also displays the disparity seen in the range of 10–40% CMB surface area coverage between low velocities and strong gradients. That is, the correlation between hot spots and velocity gradients is
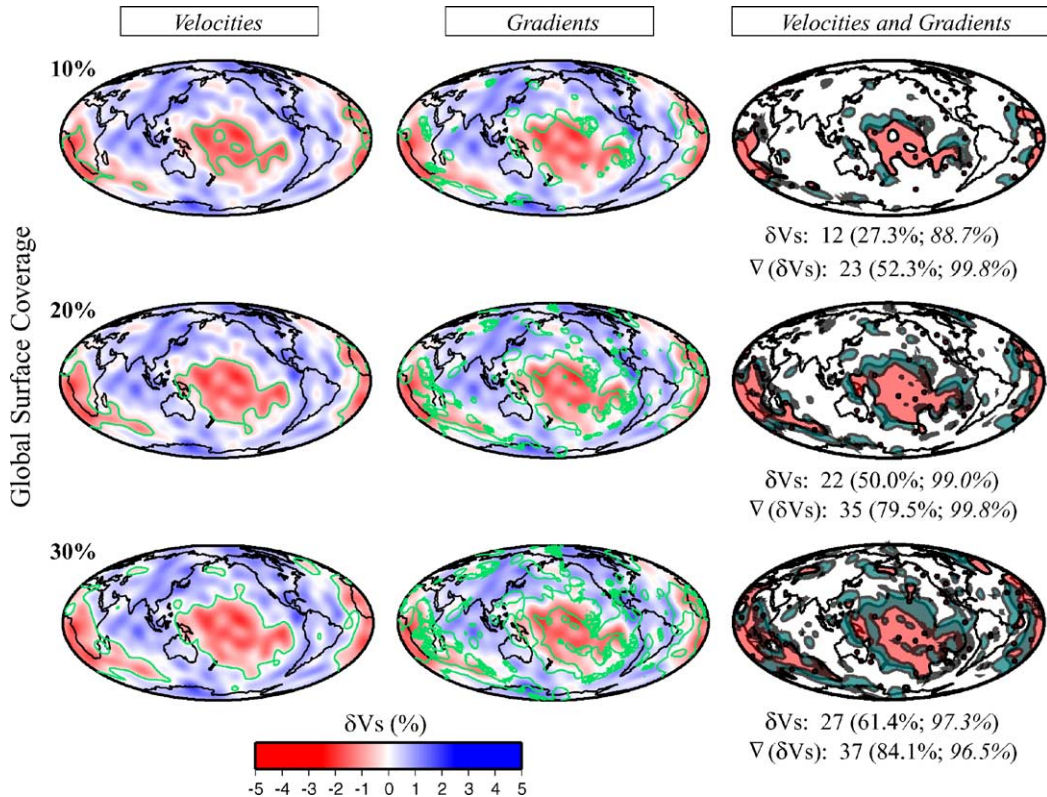
Fig. 2. Hot spot counts are shown for model S20RTS. The first column shows contour lines (green) drawn around 10, 20, and 30% CMB surface area coverage for the most anomalous low velocities. The second column has contour lines drawn around 10, 20, and 30% CMB surface area coverage for lateral S-wave velocity gradients for a 1000 km arc length with five sample points. The third column shows the CMB percent surface area coverage, contoured in the first two columns, with lowest velocities filled in red and strongest gradients filled in green. The surface locations of hot spots are plotted as red circles. The numbers beneath each drawing show for both S-wave velocity and gradient, the hot spot count and, in parenthesis, the percentage of the total amount of hot spots and the percentage of randomly rotated hot spot locations having a weaker correlation within the CMB percent surface coverage contour. All numbers are obtained using a 5° radius bin centered on the hot spot.

highest for the strongest gradients in this surface area coverage range.

In our analysis of velocity gradients, variations in hot spot hit count occur for ranges of arc length and search radius. We explored up to 2000 km arc lengths for gradient estimations. Fig. 4 shows a slightly better hot spot count for gradient calculations with a 500 km arc length than for 1000 km, however there is no significant difference between them. Gradient estimations over dimensions larger than 1000 km result in more similar hot spot hit counts between low velocities and strong gradients, which is expected because short wavelength heterogeneity is smoothed out relative to shorter arc length calculations. Hot spot counts

also depend on the size of the radius search bin used to collect the gradient and velocity values. Decreasing the search radius size reduces hot spot counts for both the velocity and gradient calculations. In particular, gradient hot spot counts decrease disproportionately relative to velocity hot spot counts, as gradients naturally possess smaller wavelength features than the velocity data from which they are derived. Conversely, increasing the size of the radius search bin, in accordance with the hot spot plume deflection calculations of Steinberger (2000), increases hot spot counts for the strongest gradients rather than the lowest velocities.

Overall hot spot hit counts for the six S-wave models analyzed are given in Tables 3 and 4. For example,
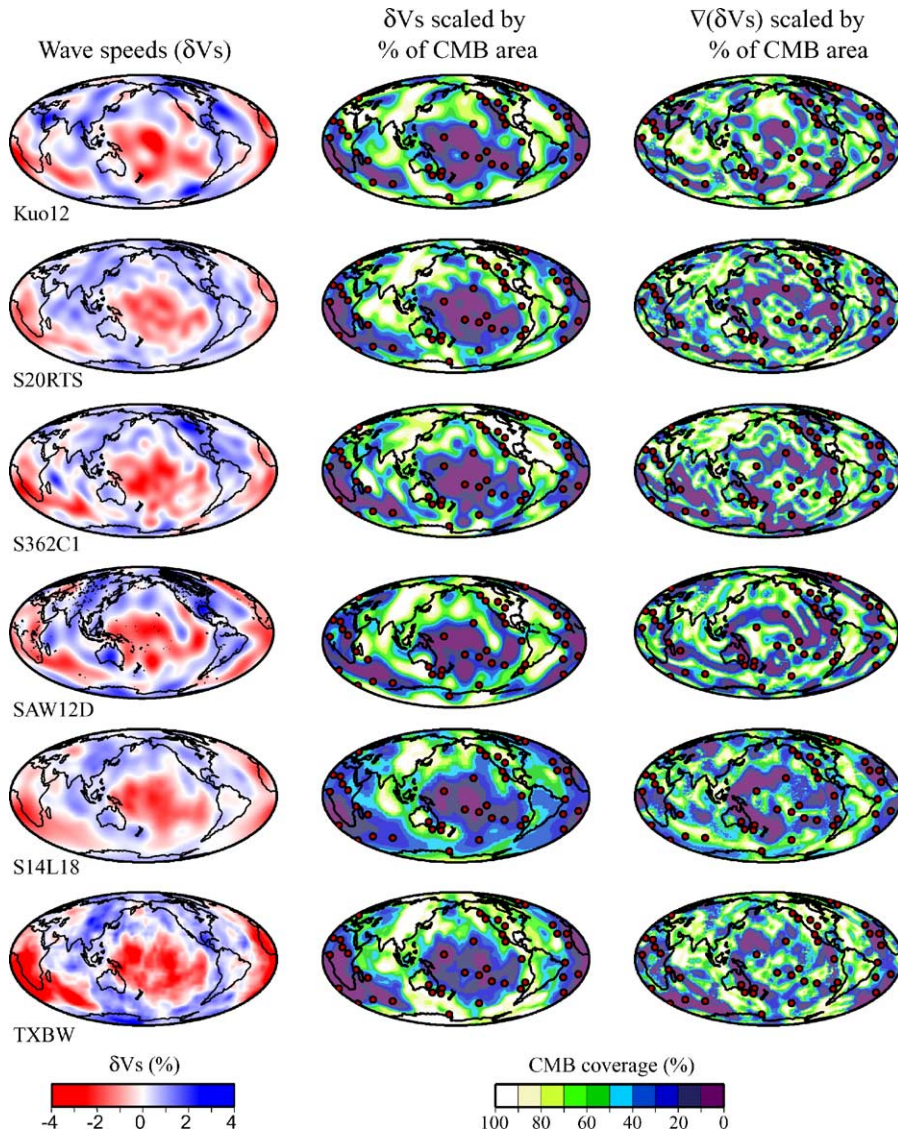
Fig. 3. The first column displays the raw S-wave velocity perturbations of the six models analyzed. The second column shows the S-wave velocity models contoured by surface area coverage of the CMB, where the most anomalous low velocities are represented by the lowest percentages. The third column shows lateral S-wave velocity gradients contoured by surface area coverage of the CMB, where the strongest gradients are represented by the lowest percentages. Lateral velocity gradients shown here are calculated for a 1000 km length of arc with five sample points used in the least square approximation. Hot spot surface locations are plotted as red circles in the second and third columns. Models are as in Table 1.

a value of 5 in Table 3 signifies that the hot spot overlies D'' S-wave heterogeneity with the magnitude ranked at 5% of the lowest velocities on Earth (i.e., 0% corresponds to the lowest velocity in D'' and 100% corresponds to the highest velocity in D''). Similarly,

a value of 5 in Table 4 signifies the hot spot overlies D'' S-wave velocity lateral gradient with the magnitude ranked at 5% of the strongest gradients on Earth. (Again, 0% corresponds to the strongest D'' lateral velocity gradients, and 100% corresponds to the weakest
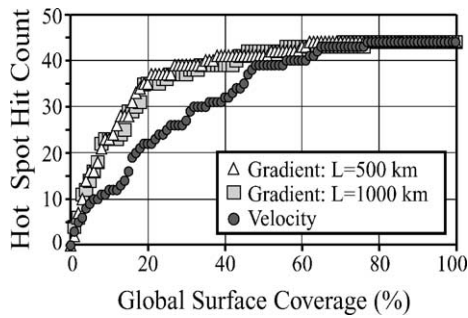
Fig. 4. The number of hot spots falling within the percentage of CMB surface area coverage are shown for model S20RTS. The triangles show the number of hot spots for a lateral velocity gradient calculation with a 500 km arc length, while the squares show the number of hot spots for a gradient calculation with a 1000 km arc length. Both gradient calculations were done with five points used in the least square approximation. The circles show the number of hot spots within the percentage of CMB surface area coverage for velocity.
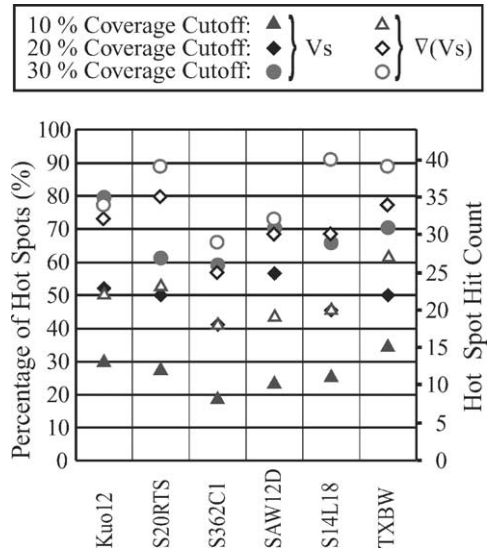

Fig. 5. The number of hot spots (hot spot hit count and percentage of total amount of hot spots) that fall within 10, 20, and 30% CMB surface area coverage for all six S-wave velocity models. The solid and open symbols show the number of hot spots falling inside the CMB percent surface area coverage for velocity and lateral S-wave velocity gradient respectively. Hot spot hit counts are shown using a 5° radius bin centered on the hot spot. Gradient calculations were done using a 500 km arc length.

gradients.) These values are presented in Fig. 5 for percent CMB surface area coverage's between 10 and 30%. This range displays a higher number of hot spots above strong gradients than for low velocities. The 10% coverage cutoff shows the greatest difference between gradient and velocity counts with an average over all models showing 49 and 46% of all hot spots falling within the gradient cutoff for 500 and 1000 km gradient measurement arcs, respectively. In comparison, only 26% of all hot spots are within 5° of the 10% of the CMB occupied by the lowest velocities.

Using the Steinberger (2000) hot spot root locations, we also calculated correlations between hot spots and either low velocities or strong gradients. As expected, hot spot roots lie closer to the lowest S-wave velocities than to strong gradients, since the roots were obtained using the assumption of a density driven flow model, where shear-wave velocities were linearly mapped to densities. The mantle wind estimates using this assumption place the source of mantle plumes near the lowest densities, corresponding to the lowest seismic velocities.

We compared the strength of correlation to hot spot buoyancy flux estimates (Sleep, 1990; Steinberger, 2000). It has been argued that flux should relate to depth of plume origin (e.g., Albers and Christensen, 1996). However, we did not observe a clear depen-

dence on flux in the correlations for either S-wave velocities or lateral S-wave velocity gradients. This is not surprising, because hot spots with relatively weak flux estimates, as compared to the Hawaiian hot spot (hot spot #18 in Fig. 1), also display hot spot traces that accurately follow plate motions. For example, Duncan and Richards (1991) pointed out that the East Australia, Tasmanid, and Lord Howe hot spots (hot spots #12, #39, and #24, Fig. 1), each with volume flux estimates of 900 kg/s (compared with 6500 kg/s for the Hawaiian hot spot (Steinberger, 2000)), accurately represent the Australian–Indian plate motion, suggesting a common source for each of them. Additionally, in the Steinberger (2000) calculation of hot spot lateral deflections, the smallest hot spots (volume flux <2000 kg/s) show a fairly even distribution of deflections ranging from 200 to 1400 km. Some of the largest hot spots (Tahiti, Marquesas, and Pitcairn, hot spots #38, #28, and #31, Fig. 1) show relatively little deflection, yet Hawaii and Macdonald (hot spot #26, Fig. 1) show as much as 700–800 km of lateral deflection.

Table 3
S-wave velocity percent coverage of CMB surface area overlain by each hot spot

Hot spot	% CMB coverage δV_s							
	SAW12D	Kuo12	S362C1	TXBW	S20RTS	S14L18	Average	S.D.
1. Azores	10.00	22.00	43.00	28.00	32.00	16.00	25.17	11.81
2. Balleny	29.00	71.00	59.00	70.00	64.00	55.00	58.00	15.49
3. Bowie	48.00	62.00	82.00	49.00	65.00	64.00	61.67	12.47
4. Cameroon	26.00	20.00	15.00	3.00	3.00	18.00	14.17	9.37
5. Canary	14.00	3.00	13.00	3.00	4.00	3.00	6.67	5.32
6. Cape Verde	16.00	7.00	10.00	3.00	8.00	11.00	9.17	4.36
7. Caroline	5.00	10.00	11.00	3.00	1.00	1.00	5.17	4.40
8. Cobb	47.00	19.00	43.00	48.00	77.00	47.00	46.83	18.44
9. Comores	44.00	28.00	40.00	23.00	26.00	22.00	30.50	9.25
10. Darfur	18.00	20.00	12.00	5.00	10.00	24.00	14.83	7.05
11. East Africa	4.00	45.00	18.00	8.00	15.00	28.00	19.67	14.95
12. East Australia	34.00	31.00	58.00	59.00	43.00	69.00	49.00	15.27
13. Easter	17.00	5.00	18.00	14.00	15.00	9.00	13.00	5.02
14. Eifel	66.00	27.00	83.00	34.00	31.00	39.00	46.67	22.56
15. Fernando	16.00	41.00	20.00	35.00	25.00	33.00	28.33	9.58
16. Galapagos	9.00	29.00	26.00	26.00	47.00	26.00	27.17	12.09
17. Guadelupe	14.00	10.00	35.00	48.00	42.00	49.00	33.00	17.06
18. Hawaii	15.00	38.00	7.00	17.00	13.00	10.00	16.67	11.04
19. Hoggar	24.00	15.00	33.00	11.00	14.00	28.00	20.83	8.80
20. Iceland	5.00	24.00	31.00	26.00	22.00	29.00	22.83	9.33
21. Jan Mayen	14.00	29.00	33.00	28.00	30.00	33.00	27.83	7.08
22. Juan Fernandez	58.00	13.00	35.00	40.00	56.00	28.00	38.33	17.10
23. Kerguelen	13.00	7.00	2.00	2.00	6.00	19.00	8.17	6.68
24. Lord Howe	5.00	19.00	24.00	24.00	36.00	37.00	24.17	11.82
25. Louisville	54.00	35.00	17.00	28.00	18.00	22.00	29.00	13.97
26. Macdonald	66.00	41.00	56.00	27.00	45.00	50.00	47.50	13.34
27. Marion	13.00	14.00	23.00	14.00	16.00	17.00	16.17	3.66
28. Marquesas	10.00	10.00	6.00	4.00	4.00	7.00	6.83	2.71
29. Meteor	22.00	17.00	15.00	5.00	23.00	19.00	16.83	6.52
30. New England	39.00	28.00	28.00	15.00	19.00	14.00	23.83	9.62
31. Pitcairn	7.00	6.00	18.00	5.00	5.00	7.00	8.00	4.98
32. Raton	65.00	24.00	79.00	64.00	40.00	62.00	55.67	19.95
33. Reunion	16.00	19.00	24.00	7.00	16.00	21.00	17.17	5.85
34. St. Helena	5.00	1.00	4.00	2.00	1.00	2.00	2.50	1.64
35. Samoa	14.00	3.00	4.00	17.00	2.00	2.00	7.00	6.69
36. San Felix	65.00	22.00	33.00	58.00	46.00	32.00	42.67	16.61
37. Socorro	14.00	15.00	47.00	49.00	46.00	55.00	37.67	18.22
38. Tahiti	15.00	6.00	12.00	6.00	1.00	3.00	7.17	5.34
39. Tasmanid	14.00	27.00	48.00	45.00	48.00	81.00	43.83	22.76
40. Tibesti	24.00	28.00	26.00	17.00	18.00	22.00	22.50	4.37
41. Trindade	25.00	31.00	14.00	25.00	31.00	23.00	24.83	6.27
42. Tristan	7.00	7.00	10.00	4.00	16.00	13.00	9.50	4.42
43. Vema	35.00	4.00	4.00	1.00	2.00	2.00	8.00	13.28
44. Yellowstone	68.00	22.00	78.00	47.00	62.00	87.00	60.67	23.37

Statistical significance testing of our correlations were performed by comparing the correlation between hot spot locations and the strength of the velocity or gradient anomaly within the radius search bin beneath them. The correlation with hot spots in their current location was compared with the correlation calculated for 10,000 pseudo-random rotations of the hot spots about three Euler angles, with the relative

Table 4
Lateral gradient percent coverage of CMB surface area overlain by each hot spot

Hot spot	% CMB coverage $\nabla (\delta V_s)$							
	SAW12D	Kuo12	S362C1	TXBW	S20RTS	S14L18	Average	S.D.
1. Azores	4.00	44.00	24.00	6.00	13.00	10.00	16.83	15.05
2. Balleny	20.00	29.00	2.00	15.00	17.00	58.00	23.50	19.02
3. Bowie	56.00	2.00	48.00	29.00	38.00	18.00	31.83	19.86
4. Cameroon	18.00	13.00	8.00	1.00	2.00	7.00	8.17	6.49
5. Canary	13.00	7.00	20.00	4.00	3.00	7.00	9.00	6.42
6. Cape Verde	8.00	5.00	7.00	1.00	4.00	3.00	4.67	2.58
7. Caroline	64.00	41.00	47.00	38.00	2.00	8.00	33.33	23.80
8. Cobb	52.00	2.00	7.00	46.00	62.00	15.00	30.67	25.69
9. Comores	3.00	26.00	11.00	12.00	13.00	9.00	12.33	7.58
10. Darfur	17.00	3.00	8.00	3.00	2.00	22.00	9.17	8.42
11. East Africa	20.00	36.00	6.00	7.00	3.00	8.00	13.33	12.55
12. East Australia	1.00	54.00	63.00	6.00	18.00	31.00	28.83	25.37
13. Easter	12.00	12.00	35.00	9.00	4.00	5.00	12.83	11.37
14. Eifel	6.00	19.00	27.00	5.00	27.00	16.00	16.67	9.69
15. Fernando	3.00	36.00	18.00	19.00	5.00	26.00	17.83	12.51
16. Galapagos	2.00	17.00	1.00	2.00	1.00	1.00	4.00	6.39
17. Guadelupe	1.00	3.00	18.00	43.00	16.00	34.00	19.17	16.68
18. Hawaii	5.00	4.00	5.00	32.00	8.00	2.00	9.33	11.27
19. Hoggar	66.00	10.00	59.00	3.00	12.00	10.00	26.67	28.01
20. Iceland	14.00	2.00	36.00	23.00	9.00	28.00	18.67	12.64
21. Jan Mayen	12.00	2.00	31.00	3.00	8.00	22.00	13.00	11.42
22. Juan Fernandez	68.00	8.00	43.00	9.00	35.00	11.00	29.00	24.16
23. Kerguelen	41.00	13.00	2.00	6.00	6.00	75.00	23.83	28.78
24. Lord Howe	7.00	5.00	7.00	8.00	7.00	2.00	6.00	2.19
25. Louisville	61.00	47.00	2.00	6.00	8.00	34.00	26.33	24.61
26. Macdonald	1.00	61.00	57.00	2.00	66.00	7.00	32.33	31.96
27. Marion	5.00	6.00	3.00	2.00	3.00	54.00	12.17	20.55
28. Marquesas	2.00	53.00	13.00	9.00	21.00	17.00	19.17	17.83
29. Meteor	7.00	7.00	7.00	0.00	3.00	18.00	7.00	6.10
30. New England	4.00	9.00	5.00	1.00	2.00	2.00	3.83	2.93
31. Pitcairn	20.00	12.00	14.00	13.00	7.00	5.00	11.83	5.34
32. Raton	11.00	6.00	12.00	46.00	9.00	12.00	16.00	14.87
33. Reunion	1.00	18.00	1.00	1.00	2.00	20.00	7.17	9.20
34. St. Helena	38.00	2.00	35.00	7.00	5.00	11.00	16.33	15.92
35. Samoa	26.00	1.00	47.00	16.00	16.00	15.00	20.17	15.38
36. San Felix	57.00	3.00	47.00	25.00	16.00	5.00	25.50	22.23
37. Socorro	1.00	3.00	21.00	13.00	11.00	34.00	13.83	12.24
38. Tahiti	34.00	38.00	43.00	10.00	21.00	56.00	33.67	16.28
39. Tasmanid	6.00	11.00	40.00	6.00	52.00	10.00	20.83	19.96
40. Tibesti	52.00	5.00	15.00	28.00	4.00	29.00	22.17	18.15
41. Trindade	3.00	56.00	29.00	28.00	17.00	29.00	27.00	17.47
42. Tristan	14.00	16.00	7.00	5.00	12.00	25.00	13.17	7.14
43. Vema	26.00	17.00	34.00	3.00	27.00	18.00	20.83	10.76
44. Yellowstone	36.00	2.00	3.00	25.00	19.00	9.00	15.67	13.44

position between hot spots maintained. For the 10% of the CMB overlain by strongest gradients averaged over all six models tested, the percentage of random hot spot locations that show a lower correlation than current hot spot locations is 94.3%. The final number in each row of Fig. 2 shows the percentage of random hot spot locations with lower correlations than current hot spot current locations for model S20RTS. For

example, at 10% CMB surface area coverage, ~89% (~11%) of randomly rotated hot spot locations show lower (higher) correlations than hot spot present locations over low velocities. Similarly, 99.8% (0.2%) of randomly rotated hot spot locations show lower (higher) correlations than hot spot present locations over strong gradients. This statistical significance testing shows that spatial grouping of current hot spot locations does not bias our results.

Our calculations for lateral S-wave velocity gradients display some model dependency, especially at shorter length scales. In order to characterize the variability of the tomographic models used, the standard deviation of the magnitude of S-wave velocities at each latitude and longitude (as scaled by CMB surface area coverage) was calculated (Fig. 6). There is good agreement between each of the models for the most anomalous low and high velocities. Model discrepancy is highest in regions with the lowest amplitude of heterogeneity. Overall, the CMB surface percent coverage (shown in Tables 3 and 4) underlying each hot spot displays consistency across all velocity models. These averages show high standard deviations for several hot spots, indicating the degree to which the tomographic models differ in these loca-

tions, and may provide indication of an upper mantle source.

As arc lengths ranging from 500 to 1500 km yield the same result for a given model, our gradient calculations are most reliable at this length scale. Calculations of gradients over smaller arc lengths tend to display more incoherency, and may only serve to highlight the small-scale differences between the different tomographic models. Longer arc lengths smooth out short wavelength heterogeneity producing more similar hot spot counts between velocity and gradient. For 500–1500 km arc lengths, all of the models display strong gradients surrounding low velocity regions, as well as coherence between the different models (Fig. 6). Nevertheless, some uncertainty exists due to variability in model resolution.

While we do not attempt to reconcile the many issues present regarding hot spot genesis, our results show that hot spot locations are better correlated with lateral S-wave velocity gradients than with S-wave velocities. This correlation does not mandate that mantle plumes feeding hot spots originate from the CMB, but it does call for further discussion regarding the possible scenarios relating to the CMB-source hypothesis. In this light, we discuss briefly several possibilities and corresponding implications of our results for plumes possibly originating at the CMB in either an isochemical or chemically heterogeneous lower mantle.

4.1. Plumes rising from an isochemical lower mantle

Hot spots may be the result of whole mantle plumes rooted at the CMB in an isochemical lower mantle. The lowest velocities in an isochemical lower mantle should be associated with the highest temperatures, with the consequence of mantle plume formation in those locations. If the tomographic models evaluated in this study are of high enough resolution to resolve CMB plume roots, several observations may be made in light of our results.

Some plumes may be rising vertically from low velocity regions detected by tomography, which may be associated with a ULVZ structure with partial melt origin (Williams and Garnero, 1996). Our results indicate that all hot spots are not necessarily located over low S-wave velocities; therefore, not all hot spots may be the result of vertically rising plumes from a
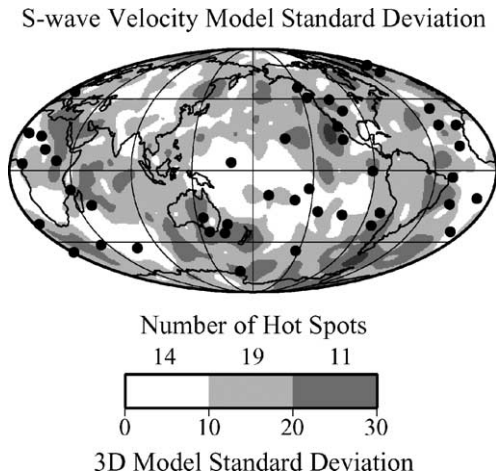

Fig. 6. The standard deviation of the six S-wave models analyzed is shown, where the magnitude of S-wave velocities are scaled by CMB surface area coverage. The number of hot spots overlying the ranges of standard deviation 0–10, 10–20, and 20–30% is indicated above the scale-bar. All standard deviation values greater than 30% (corresponding to <1% CMB surface area coverage) are shaded the darkest. Hot spots are drawn as black circles.

dynamically static isochemical lower mantle. However, plumes may be deflected in the mantle under the action of mantle winds. Alternatively, if lower mantle viscosity is too low to keep plume roots fixed, they may wander, or advect, in response to the stress field induced by whole mantle convection (Loper, 1991; Steinberger, 2000). Steinberger's (2000) calculations show density driven horizontal flow in the lower mantle that is directed inward with respect to the African and Pacific low velocity anomalies. This flow field allows for plume roots based in the lowest velocities, but through lower mantle advection are no longer underlying the surface hot spot locations. Our results are reconcilable with the possibility of upper or lower mantle advective processes shifting the plume root or surface location to non-vertical alignment. However, in the six models we analyzed the average amount of lateral deflection of all hot spot roots is ∼300–900 km (∼5–15°) for the 10–30% lowest S-wave velocities at the CMB (Fig. 7, top panel). The large uncertainties in the time for a plume to rise from the CMB makes it difficult to quantify the uncertainties in the magnitude of lateral plume deflection calculations.

Tomographic models may lack the resolution to detect lower mantle plume roots in an isochemical lower mantle, unless all plumes originate from the degree 2 low velocity features. These degree 2 low velocity features are linked to large low velocity structures rising from the CMB under Africa and the south-central Pacific, and may generate observed hot spot volcanism in those regions (Romanowicz and Gung, 2002). However, unmapped localized ULVZ structure of partial melt origin may relate to plume genesis, which would also go undetected in current tomographic studies. The observations of ULVZs (Garnero and Helmberger, 1998) and strong PKP precursors in regions not associated with anomalously low velocities in tomographic models (Wen, 2000; Niu and Wen, 2001) supports the possibility that plumes are generated at currently unmapped ULVZ locations. The recent observation of strong PKP scatterers underneath the Comores hot spot (hot spot #9, Fig. 1) (Wen, 2000) also supports this idea. ULVZs and strong PKP precursors have been found in regions of strong lateral S-wave gradients. However, spatial coverage of either ULVZ variations or PKP scatterers is far from global, which precludes comparison to global lower mantle velocities or gradients.
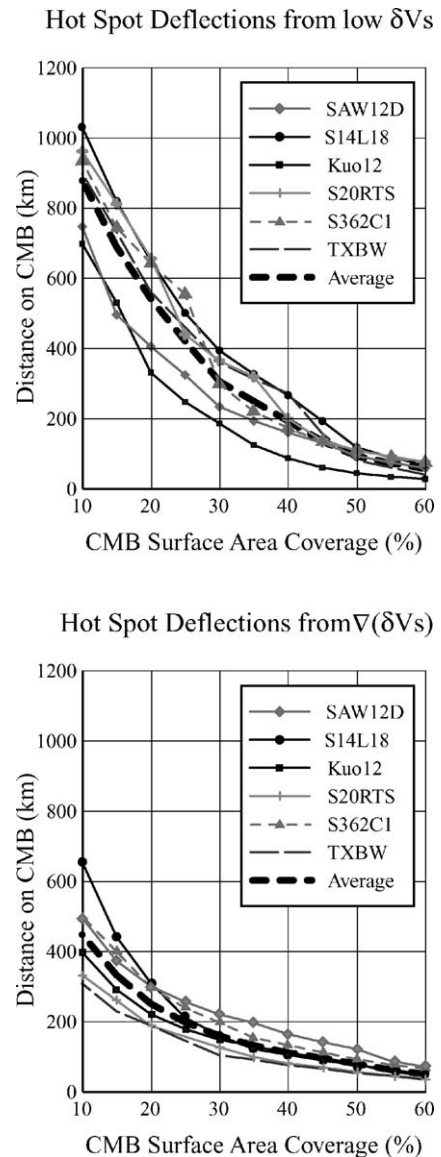

Fig. 7. The top panel shows, for each of the six tomographic models analyzed, the average distance on the CMB for all hot spots to the specified percentage of CMB surface area coverage for low S-wave velocities. The bottom panel shows the average distance on the CMB for all hot spots to the specified percentage of CMB surface area coverage from strong lateral S-wave velocity gradients.

An isochemical lower mantle cannot be completely ruled out, however, as plumes may also be initiated at strong, short-scale, lateral temperature gradients in an isochemical lower mantle (Zhao, 2001; Tan et al., 2002). Tan et al. (2002) suggests that if subducting

slabs are able to reach the CMB, then they will push aside hot mantle material and plumes will preferentially be initiated from their edges. Tomographic models may currently lack the resolution needed to characterize such short-scale variations. Nonetheless, strong short-scale temperature gradients in an isochemical lower mantle should be associated with strong lateral S-wave gradients. Tan et al. (2002) suggest that lateral temperature anomalies of ∼500 °C may exist between subducted slabs and ambient mantle material, which is comparable to temperature anomalies that may be inferred across our gradient estimation calculations (Stacey, 1995; Oganov et al., 2001). One challenge is that the strongest velocity gradients surround the lowest velocities, which are typically well separated from the high velocity D'' features typically associated with subduction. However, it is an intriguing possibility, especially considering the work of Steinberger (2000), who suggests that the lower mantle flow field is being directed inward towards the Pacific and African low velocity anomalies. It is conceivable that this lower mantle flow field could be the result of ancient subduction, and is suggested for hot spots east of South America (Ni and Helmberger, 2001). We further discuss lateral deflection of hot spot roots in the next section.

4.2. Plumes rising from a compositionally heterogeneous lower mantle

Evidence for deep mantle compositional variations has also been proposed using a variety of seismic methods at a number of spatial scales (e.g., Sylvander and Souriau, 1996; Breger and Romanowicz, 1998; Ji and Nataf, 1998a; Ishii and Tromp, 1999; van der Hilst and Karason, 1999; Wysession et al., 1999; Garnero and Jeanloz, 2000; Masters et al., 2000; Breger et al., 2001; Saltzer et al., 2001) as well as from mineralogical (e.g., Knittle and Jeanloz, 1991; Manga and Jeanloz, 1996) considerations. Dynamical simulations have also argued for either thermo-chemical boundary layer structure in D'' (e.g., Gurnis and Davies, 1986; Tackley, 1998; Kellogg et al., 1999) or argued for deep mantle compositional variation (Forte and Mitrovica, 2001). As discussed above, however, isochemical slab penetration into the deep mantle can result in plume initiation (Zhong and Gurnis, 1997; Tan et al., 2002). If lateral velocity variations are

solely thermal in origin, then these strong lateral gradient regions may imply implausibly strong thermal gradients, with peak-to-peak variations possibly nearing 2000 K (Oganov et al., 2001). This observation raises the possibility that the degree 2 low velocity features in the deep mantle have a compositional, as well as thermal, origin. To a first approximation, the strongest lateral gradients are associated with the perimeter of the lowest velocity regions, as exhibited in Fig. 2 by the strongest gradients surrounding the Pacific and southern Africa low velocity anomalies. In a compositionally heterogeneous lower mantle, many possibilities are present that relate to plume genesis.

One possibility is that compositionally distinct lower mantle material of reduced density will rise due to increased buoyancy, which may relate to plume initiation (e.g., Anderson, 1975). If the mineral phases present near the edges of such compositionally distinct features allow for eutectic melting or solvus formation, then a new post-mixing composition, if less dense, may trigger instabilities that lead to plumes. Alternatively, compositionally distinct bodies of higher thermal conductivity may increase heat transfer from the outer core, with plume formation occurring above it. Another possibility is that plume initiation may be triggered near the lowermost mantle edges of higher thermally conductive bodies. In this model, adjacent mantle material will be heated both from the CMB and the conducting chemical anomaly. However, the topography of the conductive body may extensively modify where plume conduits rise (e.g., Kellogg et al., 1999; Tackley, 2000).

Jellinek and Manga (2002) performed tank experiments indicating that a dense, low viscosity layer at the base of the mantle can become fixed over length scales longer than the rise-time of a plume. Flow driven by lateral temperature variations allows for buoyant material to rise easiest along the sloping interfaces of topographic highs of the dense, low viscosity layer. However, Jellinek and Manga (2002) suggest the topographic highs where plume initiation is easiest would to some extent be evenly distributed across an area such as the Pacific low velocity anomaly. Future dynamics experiments should further address possible scenarios that give rise to plume initiation near edges of anomalous layers.

Although our results suggest that surface locations of hot spots are more likely to overlie regions of strong

lateral S-wave velocity gradients, our results do not preclude other plume source origins. The second panel in Fig. 7 shows the average lateral deflections from vertical ascent required to explain all hot spot root locations from the strongest gradients. An average of all hot spots suggests that ∼150 to ∼450 km (∼2.5 to ∼7.5°) of lateral deflections are required if plume roots originate at the 10–30% of the CMB covered by the strongest gradients. Although this amount of deflection is considerably less than that required by deflections from the lowest velocities, some hot spots are found far from either low S-wave velocity or strong gradient regions (e.g., the Bowie and Cobb hot spots, hot spots #3 and #8, Fig. 1), indicating that some plumes may also be initiated in upper or mid-mantle source regions, or that estimations of lateral deflection are grossly underestimated.

We have also compared hot spot counts at the CMB to three other depths in the mantle: 605, 725, and 1375 km. These depths were chosen as being representative of the mantle transition zone, and of the upper and mid-lower mantle. Fig. 8 shows the number of hot spots overlying the 20% strongest gradients or lowest velocities, by surface area coverage of each of these three depth zones. The results are averaged across each of the models explored in this study (with the exclusion of the D'' model Kuo12). The highest
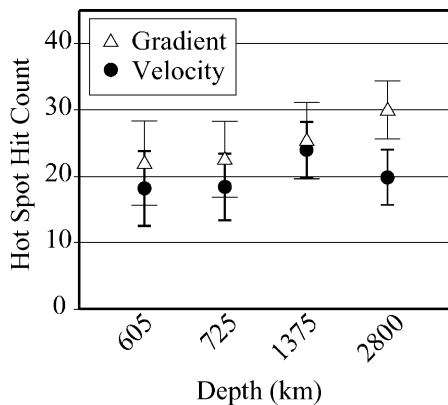

Fig. 8. Average hot spot hit counts for four zones in the mantle are shown. The circles and triangles, respectively, show the number of hot spots that overlie the most anomalous low S-wave velocities and strongest lateral S-wave velocity gradients that cover 20% of the surface area of the indicated zone. The hit counts were averaged over all models analyzed, with the exception of the D'' model Kuo12 that is only used in the deepest zone. The bars represent the standard deviation of the hot spot hit counts in each zone.

correlation is seen for hot spot surface locations and lateral gradients in the deepest layer. Additionally, the greatest disparity between hot spot counts for gradients and low S-wave velocities is also seen for the deepest layer. However, for S-wave velocities, the mid-lower mantle appears to have the highest correlation to hot spots. Fig. 8 shows that more hot spots overlie lowermost mantle low S-wave velocities than low S-wave velocities in the upper part of the lower mantle or in the transition zone.

5. Conclusions

We have shown that hot spots are more likely to overlie strong S-wave velocity lateral gradients rather than low S-wave velocity regions in the lower mantle. Nearly twice as many hot spots overlie strong gradients than low velocities occupying 10% of the surface area of the CMB. An isochemical lower mantle source to plume formation requires the presence of mantle winds and/or lower mantle advection to reconcile our correlations, unless plumes are being initiated at the edges of subducted slab material. If plumes are initiated in the lowest S-wave velocity regions of the CMB, average lateral deflections of hot spot root locations from ∼300 to 900 km at the CMB for the 10–30% of the CMB covered by the most anomalous low velocities are required. If this model of plume formation is correct, continuing improvements in whole mantle travel-time tomography and forward body wave studies will further elucidate the fine structure of such plumes. Challenges remain, however, to better document ULVZ structure, which may be related to partial melt (Williams and Garnero, 1996), as the source of mantle plumes. Further efforts to provide a more global coverage of ULVZ locations will help to resolve this issue.

On the other hand, we find that the strongest lateral S-wave velocity gradients tend to surround the large-scale lower velocity regions, with the strong gradient regions possibly signifying lateral boundaries in the deepest mantle between large-scale chemically distinct bodies, or thermal slabs. One possible origin to a compositionally distinct lower mantle is iron enrichment, which may create compositionally distinct features, resulting in a few percent reductions in velocity (Duffy and Ahrens, 1992; Wysession et al.,

1992; Williams and Garnero, 1996) and produce a stable dense feature with relatively sharp edges around its perimeter. Plumes arising from strong gradient regions would require average lateral deflections from the vertical of hot spot root locations of ∼150 to 450 km at the CMB for the 10–30% of the CMB covered by the most anomalous strong gradients. This amount of lateral deflection is significantly less than that required if plumes initiate at the lowest velocities at the CMB, however, many hot spots may not have a lower mantle source.

Plume source regions may also be located in the mid- or upper-mantle (Albers and Christensen, 1996; Anderson, 1998; Cserepes and Yuen, 2000), which may or may not be coupled to lower mantle dynamics. The number of possible plume genesis scenarios in the upper or mid-mantle is as varied as they are for the lower mantle. We have presented a better correlation between present surface locations of hot spots and deep mantle lateral S-wave velocity gradients than with S-wave velocities, and have discussed possible scenarios as to the origins of plumes that may arise from the deep mantle. However, given the wide range of uncertainties it is still impossible to ascertain the true depth origin of mantle plumes that may be responsible for surface hot spot volcanism. This issue may not be resolved until complete high-resolution images of plumes from top to bottom are successfully obtained.

Acknowledgements

References

Albarede, F., van der Hilst, R.D., 2002. Zoned mantle convection. Phil. Trans. R. Soc. London Ser. A: Math. Phys. Eng. Sci. 360 (1800), 2569–2592.

Albers, M., Christensen, U.R., 1996. The excess temperature of plumes rising from the core–mantle boundary. Geophys. Res. Lett. 23 (24), 3567–3570.

Anderson, D.L., 1975. Chemical plumes in mantle. Geol. Soc. Am. Bull. 86 (11), 1593–1600.

Anderson, D.L., 1998. The scales of mantle convection. Tectonophysics 284 (1/2), 1–17.

Bijwaard, H., Spakman, W., Engdahl, E.R., 1998. Closing the gap between regional and global travel time tomography. J. Geophys. Res.-Solid Earth 103 (B12), 30055–30078.

Bijwaard, H., Spakman, W., 1999. Tomographic evidence for a narrow whole mantle plume below Iceland. Earth Planet. Sci. Lett. 166 (3/4), 121–126.

Brandon, A.D., Walker, R.J., Morgan, J.W., Norman, M.D., Prichard, H.M., 1998. Coupled Os-186 and Os-187 evidence for core–mantle interaction. Science 280 (5369), 1570–1573.

Breger, L., Romanowicz, B., 1998. Three-dimensional structure at the base of the mantle beneath the central Pacific. Science 282 (5389), 718–720.

Breger, L., Romanowicz, B., Ng, C., 2001. The Pacific plume as seen by S, ScS, and SKS. Geophys. Res. Lett. 28 (9), 1859–1862.

Bunge, H.P., Richards, M.A., 1996. The origin of large scale structure in mantle convection: effects of plate motions and viscosity stratification. Geophys. Res. Lett. 23 (21), 2987–2990.

Castle, J.C., Creager, K.C., Winchester, J.P., van der Hilst, R.D., 2000. Shear wave speeds at the base of the mantle. J. Geophys. Res.-Solid Earth 105 (B9), 21543–21557.

Clouard, V., Bonneville, A., 2001. How many Pacific hotspots are fed by deep-mantle plumes? Geology 29 (8), 695–698.

Cserepes, L., Yuen, D.A., 2000. On the possibility of a second kind of mantle plume. Earth Planet. Sci. Lett. 183 (1/2), 61–71.

Davies, G.F., 1988. Ocean bathymetry and mantle convection. 1. Large-scale flow and hotspots. J. Geophys. Res.-Solid Earth Planets 93 (B9), 10467–10480.

Duffy, T.S., Ahrens, T.J., 1992. Sound velocities at high-pressure and temperature and their geophysical implications. J. Geophys. Res.-Solid Earth 97 (B4), 4503–4520.

Duncan, R.A., Richards, M.A., 1991. Hotspots, mantle plumes, flood basalts, and true polar wander. Rev. Geophys. 29 (1), 31–50.

Dziewonski, A.M., 1984. Mapping the lower mantle—determination of lateral heterogeneity in P-velocity up to degree and order-6. J. Geophys. Res. 89 (NB7), 5929–5952.

Forte, A.M., Mitrovica, J.X., 2001. Deep-mantle high-viscosity flow and thermochemical structure inferred from seismic and geodynamic data. Nature 410 (6832), 1049–1056.

Foulger, G.R., et al., 2001. Seismic tomography shows that upwelling beneath Iceland is confined to the upper mantle. Geophys. J. Int. 146 (2), 504–530.

Garnero, E.J., Helmberger, D.V., 1998. Further structural constraints and uncertainties of a thin laterally varying ultralow-velocity layer at the base of the mantle. J. Geophys. Res.-Solid Earth 103 (B6), 12495–12509.

Garnero, E.J., Jeanloz, R., 2000. Fuzzy patches on the Earth's core–mantle boundary? Geophys. Res. Lett. 27 (17), 2777–2780.

Goes, S., Spakman, W., Bijwaard, H., 1999. A lower mantle source for central European volcanism. Science 286 (5446), 1928–1931.

Gorbatov, A., Fukao, Y., Widiyantoro, S., Gordeev, E., 2001. Seismic evidence for a mantle plume oceanwards of the Kamchatka–Aleutian trench junction. Geophys. J. Int. 146 (2), 282–288.

Grand, S.P., 1994. Mantle shear structure beneath the America and surrounding oceans. J. Geophys. Res.-Solid Earth 99 (B6), 11591–11621.

Grand, S.P., van der Hilst, R.D., Widiyantoro, S., 1997. Global seismic tomography: a snapshot of convection in the earth. GSA Today 7 (4), 1–7.

Grand, S.P., 2002. Mantle shear-wave tomography and the fate of subducted slabs. Phil. Trans. R. Soc. London Ser. A: Math. Phys. Eng. Sci. 360 (1800), 2475–2491.

Gu, Y.J., Dziewonski, A.M., Su, W.J., Ekstrom, G., 2001. Models of the mantle shear velocity and discontinuities in the pattern of lateral heterogeneities. J. Geophys. Res.-Solid Earth 106 (B6), 11169–11199.

Gurnis, M., Davies, G.F., 1986. Mixing in numerical-models of mantle convection incorporating plate kinematics. J. Geophys. Res.-Solid Earth Planets 91 (B6), 6375–6395.

Hager, B.H., Clayton, R.W., Richards, M.A., Comer, R.P., Dziewonski, A.M., 1985. Lower mantle heterogeneity, dynamic topography and the geoid. Nature 313 (6003), 541–546.

Hanan, B.B., Graham, D.W., 1996. Lead and helium isotope evidence from oceanic basalts for a common deep source of mantle plumes. Science 272 (5264), 991–995.

Hart, S.R., Hauri, E.H., Oschmann, L.A., Whitehead, J.A., 1992. Mantle plumes and entrainment—isotopic evidence. Science 256 (5056), 517–520.

Helmberger, D.V., Wen, L., Ding, X., 1998. Seismic evidence that the source of the Iceland hotspot lies at the core–mantle boundary. Nature 396 (6708), 251–255.

Hofmann, A.W., 1997. Mantle geochemistry: the message from oceanic volcanism. Nature 385 (6613), 219–229.

Ishii, M., Tromp, J., 1999. Normal-mode and free-air gravity constraints on lateral variations in velocity and density of Earth's mantle. Science 285 (5431), 1231–1236.

Jellinek, A.M., Manga, M., 2002. The influence of a chemical boundary layer on the fixity, spacing and lifetime of mantle plumes. Nature 418 (6899), 760–763.

Ji, Y., Nataf, H.C., 1998a. Detection of mantle plumes in the lower mantle by diffraction tomography: theory. Earth Planet. Sci. Lett. 159 (3/4), 87–98.

Ji, Y., Nataf, H.C., 1998b. Detection of mantle plumes in the lower mantle by diffraction tomography: Hawaii. Earth Planet. Sci. Lett. 159 (3/4), 99–115.

Kellogg, L.H., Hager, B.H., van der Hilst, R.D., 1999. Compositional stratification in the deep mantle. Science 283 (5409), 1881–1884.

Knittle, E., Jeanloz, R., 1991. Earths core–mantle boundary—results of experiments at high-pressures and temperatures. Science 251 (5000), 1438–1443.

Kuo, B.Y., Garnero, E.J., Lay, T., 2000. Tomographic inversion of S–SKS times for shear velocity heterogeneity in D'': degree 12 and hybrid models. J. Geophys. Res.-Solid Earth 105 (B12), 28139–28157.

Li, X.D., Romanowicz, B., 1996. Global mantle shear velocity model developed using nonlinear asymptotic coupling theory. J. Geophys. Res.-Solid Earth 101 (B10), 22245–22272.

Lithgow-Bertelloni, C., Richards, M.A., 1998. The dynamics of cenozoic and mesozoic plate motions. Rev. Geophys. 36 (1), 27–78.

Loper, D.E., Stacey, F.D., 1983. The dynamical and thermal structure of deep mantle plumes. Phys. Earth Planet. Int. 33 (4), 304–317.

Loper, D.E., 1991. Mantle Plumes. Tectonophysics 187 (4), 373–384.

Manga, M., Jeanloz, R., 1996. Implications of a metal-bearing chemical boundary layer in D'' for mantle dynamics. Geophys. Res. Lett. 23 (22), 3091–3094.

Masters, G., Laske, G., Bolton, H., Dziewonski, A.M., 2000. The Relative Behavior of Shear Velocity, Bulk Sound Speed, and Compressional Velocity in the Mantle: Implications for Chemical and Thermal Structure, Earth's Deep Interior: Mineral Physics and Tomography From the Atomic to the Global Scale. American Geophysical Union, Washington, DC, pp. 63–87.

Megnin, C., Romanowicz, B., 2000. The three-dimensional shear velocity structure of the mantle from the inversion of body, surface and higher-mode waveforms. Geophys. J. Int. 143 (3), 709–728.

Morgan, W.J., 1971. Convection plumes in the lower mantle. Nature 230, 42–43.

Morgan, W.J., 1972. Deep mantle convection plumes and plate motions. Am. Assoc. Petrol. Geol. Bull. 56 (2), 203–213.

Nataf, H.C., Vandecar, J., 1993. Seismological detection of a mantle plume. Nature 364 (6433), 115–120.

Nataf, H.C., 2000. Seismic imaging of mantle plumes. Annu. Rev. Earth Planet. Sci. 28, 391–417.

Ni, S.D., Ding, X.M., Helmberger, D.V., Gurnis, M., 1999. Low-velocity structure beneath Africa from forward modeling. Earth Planet. Sci. Lett. 170 (4), 497–507.

Ni, S.D., Helmberger, D.V., 2001. Horizontal transition from fast to slow structures at the core–mantle boundary; South Atlantic. Earth Planet. Sci. Lett. 187 (3/4), 301–310.

Niu, F.L., Wen, L.X., 2001. Strong seismic scatterers near the core–mantle boundary west of Mexico. Geophys. Res. Lett. 28 (18), 3557–3560.

Niu, F.L., Solomon, S.C., Silver, P.G., Suetsugu, D., Inoue, H., 2002. Mantle transition-zone structure beneath the South Pacific Superswell and evidence for a mantle plume underlying the Society hotspot. Earth Planet. Sci. Lett. 198 (3/4), 371–380.

Oganov, A.R., Brodholt, J.P., Price, G.D., 2001. The elastic constants of $MgSiO_3$ perovskite at pressures and temperatures of the Earth's mantle. Nature 411 (6840), 934–937.

Ribe, N.M., Devalpine, D.P., 1994. The global hotspot distribution and instability of D''. Geophys. Res. Lett. 21 (14), 1507–1510.

Ribe, N.M., Christensen, U.R., 1994. 3-Dimensional modeling of plume–lithosphere interaction. J. Geophys. Res.-Solid Earth 99 (B1), 669–682.

Ritsema, J., van Heijst, H.J., Woodhouse, J.H., 1999. Complex shear wave velocity structure imaged beneath Africa and Iceland. Science 286 (5446), 1925–1928.

Ritsema, J., van Heijst, H.-J., 2000. Seismic imaging of structural heterogeneity in earth's mantle: evidence for large-scale mantle flow. Sci. Prog. 83, 243–259.

Romanowicz, B., Gung, Y.C., 2002. Superplumes from the core–mantle boundary to the lithosphere: implications for heat flux. Science 296 (5567), 513–516.

Saltzer, R.L., van der Hilst, R.D., Karason, H., 2001. Comparing P and S wave heterogeneity in the mantle. Geophys. Res. Lett. 28 (7), 1335–1338.

Seidler, E., Jacoby, W.R., Cavsak, H., 1999. Hotspot distribution, gravity, mantle tomography: evidence for plumes. J. Geodyn. 27 (4/5), 585–608.

Shen, Y., et al., 2002. Seismic evidence for a tilted mantle plume and north–south mantle flow beneath Iceland. Earth Planet. Sci. Lett. 197 (3/4), 261–272.

Sleep, N.H., 1990. Hotspots and mantle plumes—some phenomenology. J. Geophys. Res.-Solid Earth Planets 95 (B5), 6715–6736.

Stacey, F.D., 1995. Theory of thermal and elastic properties of the lower mantle and core. Phys. Earth Planet. Int. 89 (3/4), 219–245.

Steinberger, B., 2000. Plumes in a convecting mantle: models and observations for individual hotspots. J. Geophys. Res.-Solid Earth 105 (B5), 11127–11152.

Su, W.J., Woodward, R.L., Dziewonski, A.M., 1994. Degree-12 model of shear velocity heterogeneity in the mantle. J. Geophys. Res.-Solid Earth 99 (B4), 6945–6980.

Sylvander, M., Souriau, A., 1996. P-velocity structure of the core–mantle boundary region inferred from PKP (AB)–PKP (BC) differential travel times. Geophys. Res. Lett. 23 (8), 853–856.

Tackley, P.J., 1998. Three-dimensional simulations of mantle convection with a thermochemical CMB boundary layer: D''? In: Gurnis, M., Wysession, M.E., Knittle, E., Buffet, B.A. (Eds.), The Core–Mantle Boundary Region. American Geophysical Union, Washington, DC, pp. 231–253.

Tackley, P.J., 2000. Mantle convection and plate tectonics: toward an integrated physical and chemical theory. Science 288 (5473), 2002–2007.

Tan, E., Gurnis, M., Han, L.J., 2002. Slabs in the lower mantle and their modulation of plume formation. Geochemistry Geophys. Geosyst. 3, 1–24.

van der Hilst, R.D., Widiyantoro, S., Engdahl, E.R., 1997. Evidence for deep mantle circulation from global tomography. Nature 386 (6625), 578–584.

van der Hilst, R.D., Karason, H., 1999. Compositional heterogeneity in the bottom 1000 km of Earth's mantle: toward a hybrid convection model. Science 283 (5409), 1885–1888.

Vogt, P.R., 1981. On the applicability of thermal conduction models to mid-plate volcanism—comments. J. Geophys. Res. 86 (B2), 950–960.

Wen, L.X., Anderson, D.L., 1995. The fate of slabs inferred from seismic tomography and 130 million years of subduction. Earth Planet. Sci. Lett. 133 (1/2), 185–198.

Wen, L.X., Anderson, D.L., 1997. Slabs, hotspots, cratons and mantle convection revealed from residual seismic tomography in the upper mantle. Phys. Earth Planet. Int. 99 (1/2), 131–143.

Wen, L.X., 2000. Intense seismic scattering near the Earth's core–mantle boundary beneath the Comoros hotspot. Geophys. Res. Lett. 27 (22), 3627–3630.

Williams, Q., Garnero, E.J., 1996. Seismic evidence for partial melt at the base of Earth's mantle. Science 273 (5281), 1528–1530.

Williams, Q., Revenaugh, J., Garnero, E., 1998. A correlation between ultra-low basal velocities in the mantle and hot spots. Science 281 (5376), 546–549.

Wolfe, C.J., Bjarnason, I.T., VanDecar, J.C., Solomon, S.C., 1997. Seismic structure of the Iceland mantle plume. Nature 385 (6613), 245–247.

Wysession, M.E., Okal, E.A., Bina, C.R., 1992. The structure of the core–mantle boundary from diffracted waves. J. Geophys. Res.-Solid Earth 97 (B6), 8749–8764.

Wysession, M.E., et al., 1999. Lateral variations in compressional/shear velocities at the base of the mantle. Science 284 (5411), 120–125.

Zhao, D., 2001. Seismic structure and origin of hotspots and mantle plumes. Earth Planet. Sci. Lett. 192 (3), 251–265.

Zhong, S., Gurnis, M., 1997. Dynamic interaction between tectonic plates, subducting slabs, and the mantle. Earth Interact. 1, 1–18.